Available online at https://link.springer.com/journal/42241
http://www.jhydrodynamics.com
Journal of Hydrodynamics, 2025, 37(2): 246-255
https://doi.org/10.1007/s42241-025-0023-4

Analysis of flow structure and air entrainment around a shallowly submerged hydrofoil based on third-generation vortex identification

Yu-ming Shao[1], Bo-wei Song[2], Jian-hua Wang[1], De-cheng Wan[1*]
1. *Computational Marine Hydrodynamics Lab (CMHL), School of Ocean and Civil Engineering, Shanghai Jiao Tong University, Shanghai 200240, China*
2. *Ningbo Dagang Pilotage Co., Ltd., Ningbo 315020, China*

(Received October 9, 2024, Revised October 23, 2024, Accepted October 24, 2024, Published online August 4, 2025)

Abstract: A shallowly submerged hydrofoil often induces disturbances on the free water surface by generating numerous vortex structures, leading to phenomena such as wave breaking and droplet splashing. These phenomena involve various physical mechanisms. In this study, the third-generation vortex identification technique, Liutex, is employed to perform a detailed analysis of the vortex structures generated by the hydrofoil near the free surface. It is observed that these coherent vortex structures strongly entrain surrounding fluid, resulting in air entrainment and bubble sweep-down phenomena. We analyze the bubble dynamics in terms of bubble number density, volume distribution, and number distribution, revealing the dynamic characteristics of bubbles under the influence of vortex structures. Additionally, by tracking the vortex structures, two distinct forms of air entrainment are identified. The analysis of bubble motion using Liutex demonstrates the evolution and distribution patterns of bubble sizes in the turbulent flow field. The results indicate that the third-generation vortex identification technique, Liutex, effectively explains the mechanisms behind free surface breaking induced by the shallowly submerged hydrofoil.

Key words: Third-generation vortex identification, Liutex, coherent vortex structures, breaking waves

0. Introduction

There are many distinct types of vortex structures with different scales and strengths in both nature and engineering, particularly in turbulent flow fields. These vortex structures disturb the flow field and are crucial to the generation and evolution of turbulence[1]. As a result, it is essential to accurately identify vortex structures in order to comprehend the flow mechanism, resolve turbulence issues, and implement flow control.

In the early days, the magnitude of vorticity (gradient tensor of velocity) is taken as the strength of vortex structure, but it is found that its physical significance is not clear in the practical application, and causes a lot of misconceptions in turbulence research. Therefore, the second generation of vortex identification methods such as Q, Δ, λ_2 and λ_{ci} have been developed[2]. These methods are either a modification of the Cauchy-Stokes decomposition or based on velocity gradient tensor eigenvalues. The second generation vortex identification methods have improved the understanding of vortex structure to some extent. However, it has the disadvantages of threshold selection, the recognitional results are contaminated by shear, and it cannot recognize strong and weak vortices at the same time, etc. In 2016, Chaoqun Liu's team proposed Ω vortex identification method, which is firstly proposed to decompose the vortex volume into rotating and non-rotating parts, and to overcome the problem of threshold selection in the second generation of vortex identification method[3]. In 2017, Liu named the rotating part "Rortex", whose direction represents the local rotation axis and whose magnitude represents the rotation angular velocity[4]. In 2018, Rortex was renamed to Liutex vector, and for more details, please refer to the paper[5].

With the development of computational resources and numerical techniques in recent years, attention has gradually begun to focus on bubble entrainment due to wave breaking, and the subsequent downward sweeping motion of the bubbles. Due to the complexity of the wave breaking mechanism and the

Project supported by the National Natural Science Foundation of China (Grant Nos. 52131102, 52471335).
Biography: Yu-ming Shao (1998-), Male, Ph. D.,
E-mail: yuming_shao@sjtu.edu.cn
Corresponding author: De-cheng Wan,
E-mail: dcwan@sjtu.edu.cn

turbulence characteristics of the bubble entrainment that occurs after wave breaking, analyzing this phenomenon is still a challenging task. Vortex identification methods have been applied to reveal the flow properties of breaking waves. Di Giorgio et al.[6] used λ_{ci} - method to extract coherent vortex structures, such as vortex tubes and vortex sheets, during the breaking process of three-dimensional Stokes waves. They investigated the different presentation of vortex structures in different Reynolds numbers. They also revealed the link between vortex structures and energy dissipation and emphasized that wave dissipation is mainly due to vortex sheets, while vortex tubes mainly control intermittency. Li et al.[7] employed the Q - method to investigate the temporal evolution of turbulent vortex structures around hydrofoils. They discovered that the quasi-ordered structures have a strong capacity for entraining fluid, which induces a swirling effect on the surrounding fluid. A typical manifestation in wedge-shaped hydraulic jumps is the complex air entrainment process in the flow separation zone and shoulder wave breaking region. Hu et al.[8-10] utilized the Liutex-method to study the vortex structures in wave breaking induced by plate towing. Furthermore, they developed the Liutex force model[11-13] to investigate the interaction between the free surface and vortices, and illustrated the effectiveness of mitigating or controlling bubble entrainment.

This paper investigates the phenomenon of free surface breaking induced by a shallowly submerged hydrofoil. The third-generation vortex identification method is employed to analyze the flow field structures and bubble entrainment.

1. Mathematical formulations

1.1 *Numerical methods*

This study is based on the incompressible two-phase flow solver, Basilisk Flow Solver[14-15], which has been validated in numerous two-phase flow problems[16-18]. The governing equations solved in this study are as follows:

$$\rho\left[\frac{\partial \boldsymbol{u}}{\partial t}+(\boldsymbol{u}\cdot\nabla)\boldsymbol{u}\right]=-\nabla p+\nabla\cdot(2\mu\boldsymbol{D})+\rho\boldsymbol{g}+\boldsymbol{a} \tag{1}$$

$$\nabla\cdot\boldsymbol{u}=0 \tag{2}$$

where $\boldsymbol{u}$ is the fluid velocity, $\boldsymbol{D}$ is the deformation tensor defined as $D_{ij}=(\partial_i u_j+\partial_j u_i)/2$, ρ is the fluid density and p is the pressure. The term $\boldsymbol{a}=\rho\boldsymbol{g}+\boldsymbol{F}_\sigma$ is the source term, which includes the contributions of gravity and surface tension in this study.

To accurately capture the free surface, the coupled level-set and volume of fluid (CLSVOF) method is employed in this paper. This method combines the mass conservation advantages of the VOF method with the precise curvature computation of the level-set method. The fluid transport equation for this method is as follows:

$$\partial_t f+\nabla\cdot(f\boldsymbol{u})=0 \tag{3}$$

$$\partial_t \phi+\nabla\cdot(\phi\boldsymbol{u})=0 \tag{4}$$

where f is the volume fraction in the VOF method, ϕ is the distance function in the level-set method. The surface tension at the free surface is computed as follows:

$$\boldsymbol{F}_\sigma=\sigma\kappa(\phi)\delta_s\boldsymbol{n} \tag{5}$$

where σ is the surface tension coefficient, κ is the curvature of the free surface, δ_s is the Dirac function of the interface and $\boldsymbol{n}$ is the surface normal.

1.2 *Liutex vortex identification method*

For the specific definition of Liutex, please refer to the papers[4-5, 19-20]. This section will explain how to implement the Liutex computation within the Basilisk Flow Solver. We need to use the "foreach ( )" function to go through each grid and perform the following calculation for each grid:

(1) Compute the velocity gradient tensor $\boldsymbol{J}$

$$\boldsymbol{J}=\nabla\boldsymbol{u}=\begin{pmatrix}\frac{\partial u_x}{\partial x} & \frac{\partial u_x}{\partial y} & \frac{\partial u_x}{\partial z}\\ \frac{\partial u_y}{\partial x} & \frac{\partial u_y}{\partial y} & \frac{\partial u_y}{\partial z}\\ \frac{\partial u_z}{\partial x} & \frac{\partial u_z}{\partial y} & \frac{\partial u_z}{\partial z}\end{pmatrix} \tag{6}$$

(2) Compute the eigenvalues λ_i and the eigenvector $\boldsymbol{v}_i$ of the velocity gradient tensor

$$J_i=\lambda_i\boldsymbol{v}_i \tag{7}$$

It should be emphasized that in the work by Liu et al.[4, 21], the solutions are obtained using the linear algebra library LAPACK. In this study, we analytically solve the eigenvalues of the 3×3 matrix $\boldsymbol{J}$ using the Cardano formula.

(3) Construct the rotation matrix $\boldsymbol{Q}$

According to the principal eigenvector $\boldsymbol{v}_3$ (cor-

responding to the largest eigenvalue), the rotation matrix is constructed, and the velocity gradient tensor is converted to the rotating base.

First define the unit vector $\boldsymbol{v}_z$

$$\boldsymbol{v}_z = \begin{pmatrix} 0 \\ 0 \\ 1 \end{pmatrix} \tag{8}$$

Calculate the rotation axis $\boldsymbol{\gamma}$ and rotation angle ϕ

$$\boldsymbol{\gamma} = \frac{\boldsymbol{v}_z \times \boldsymbol{v}_3}{|\boldsymbol{v}_z \times \boldsymbol{v}_3|} \tag{9}$$

$$\cos(\phi) = \frac{\boldsymbol{v}_z \cdot \boldsymbol{v}_3}{|\boldsymbol{v}_z||\boldsymbol{v}_3|} \tag{10}$$

$$\phi = \arccos[\cos(\phi)] \tag{11}$$

Construct the orthogonal matrix $\boldsymbol{Q}^*$

$$\boldsymbol{Q}^* = (\boldsymbol{q}_1, \boldsymbol{q}_2, \boldsymbol{q}_3) \tag{12}$$

$$\boldsymbol{q}_1 = \begin{pmatrix} \cos(\phi) + \gamma_x^2[1-\cos(\phi)] \\ \gamma_y\gamma_x[1-\cos(\phi)] + \gamma_z \sin(\phi) \\ \gamma_z\gamma_x[1-\cos(\phi)] - \gamma_y \sin(\phi) \end{pmatrix} \tag{13}$$

$$\boldsymbol{q}_2 = \begin{pmatrix} \gamma_x\gamma_y[1-\cos(\phi)] - \gamma_z \sin(\phi) \\ \cos(\phi) + \gamma_y^2[1-\cos(\phi)] \\ \gamma_z\gamma_y[1-\cos 1-\cos(\phi)] + \gamma_x \sin 1-\cos(\phi) \end{pmatrix} \tag{14}$$

$$\boldsymbol{q}_3 = \begin{pmatrix} \gamma_x\gamma_z[1-\cos(\phi)] + \gamma_y \sin(\phi) \\ \gamma_y\gamma_z[1-\cos(\phi)] - \gamma_x \sin(\phi) \\ \cos(\phi) + \gamma_z^2[1-\cos(\phi)] \end{pmatrix} \tag{15}$$

Construct the final rotation matrix $\boldsymbol{Q}$ based on the determinant of $\boldsymbol{Q}^*$

$$\boldsymbol{Q} = (\boldsymbol{Q}^*)^{\mathrm{T}}, \quad |\boldsymbol{Q}^*| = 1 \tag{16a}$$

$$\boldsymbol{Q} = \boldsymbol{M}(\boldsymbol{Q}^*)^{\mathrm{T}}, \quad |\boldsymbol{Q}^*| = -1, \quad \boldsymbol{M} = \begin{pmatrix} 1 & 0 & 0 \\ 0 & 1 & 0 \\ 0 & 0 & -1 \end{pmatrix} \tag{16b}$$

(4) Calculate the new velocity gradient tensor $\boldsymbol{J}'$ under the locally rotating base

$$\boldsymbol{J}' = \boldsymbol{Q}\boldsymbol{J}\boldsymbol{Q}^{\mathrm{T}} \tag{17}$$

(5) Calculate Liutex value

Calculate α and β

$$\alpha = 0.5\sqrt{(J'_{xx} - J'_{yy})^2 + (J'_{xy} + J'_{yx})^2} \tag{18}$$

$$\beta = 0.5(J'_{yx} - J'_{xy}) \tag{19}$$

Calculate the value of Liutex R

$$R = 2(\beta - \alpha), \quad \alpha^2 - \beta^2 < 0, \quad \beta > 0 \tag{20a}$$

$$R = 2(\beta + \alpha), \quad \alpha^2 - \beta^2 < 0, \quad \beta < 0 \tag{20b}$$

$$R = 0, \quad \alpha^2 - \beta^2 \geq 0 \tag{20c}$$

(6) Compute the Liutex vector

Liutex vector $\boldsymbol{R} = R\boldsymbol{v}_3$

The Modified Liutex-Omega method is further applied to normalize Liutex values

$$\Omega_R = \frac{\beta^2}{\beta^2 + \alpha^2 + \lambda_{cr}^2 + 0.5\lambda_r^2 + \varepsilon} \tag{21}$$

where λ_{cr} and λ_r are real part of conjugate complex eigenvalues and real eigenvalues of velocity gradient tensor, $\varepsilon = b_0 \max(\beta^2 - \alpha^2, 0)$ is a small parameter to avoid division by zero and $b_0 = 10^{-6}$ is a small constant.

The entire computational process is shown in Table 1. At the moments when Liutex needs to be calculated, the following computational steps can be added to the Basilisk Flow Solver.

Table 1 Liutex vortex identification method calculation steps in the Basilisk Flow Solver

	Calculation procedure
1	Initialize the global vector $\boldsymbol{R}$, scalar Ω_R
2	**For** each cell in mesh **do**
3	Calculate the velocity gradient tensor $\boldsymbol{J}$
4	Calculate the eigenvalues and eigenvectors
5	**if** a real root and a pair of conjugate virtual roots **then**
6	Calculate rotation matrix Q
7	Calculate velocity gradient tensor $\boldsymbol{J}' = Q\boldsymbol{J}Q^{\mathrm{T}}$
8	Calculate α and β
9	Compute Liutex $\boldsymbol{R}$, Ω_R
10	**end if**
11	**end for**

2. Numerical setup

This study primarily investigates the phenomenon of free wave breaking induced by the NACA0012 hydrofoil at different shallow submersions. The initial experiments were conducted by Duncan[22]. While numerous scholars have performed numerical simulations on two-dimensional cases[23-24], most of these studies focus only on macro quantities such as the forces acting on the hydrofoils and lack consideration of phenomena such as bubble entrainment and bubble sweep-down generated by wave breaking. This paper will conduct numerical simulations on three-dimensional cases. The parameters for the NACA0012 hydrofoil are shown in Table 2.

Table 2 NACA0012 hydrofoil geometry model parameters

Parameters	Value
Angle of attack/°	10
Chord length, c / m	1
Span length, L / m	0.2
Velocity of incoming flow, U / (m·s^{-1})	1.789

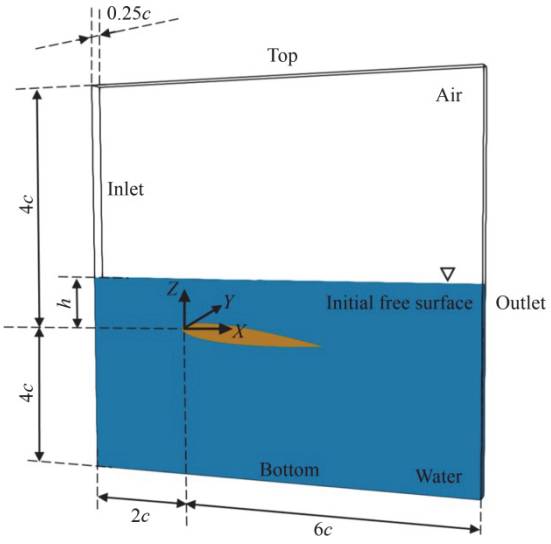

Fig. 1 The computational domain

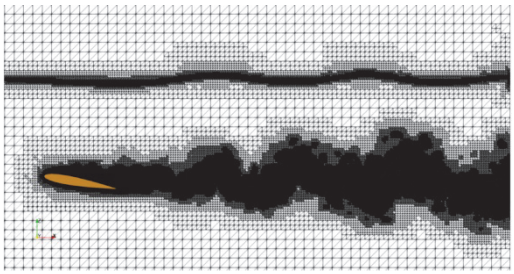

Fig. 2 Schematic diagram of adaptive grid refinement

The initial computational setup is shown in Fig. 1. The inlet boundary is located $2c$ upstream of the hydrofoil's leading edge and is set as a Dirichlet velocity boundary. The outlet boundary is positioned $6c$ away from the hydrofoil to allow sufficient evolution of the wake and is set as the Neumann conditions. The top and bottom boundaries are $4c$ away from the hydrofoil and are set as no-slip conditions. The width of the entire computational domain is $0.25c$, with the front and back boundaries set as symmetric boundary conditions. The distance from the hydrofoil's leading edge to the free surface is denoted as h, which represents the submersion depth.

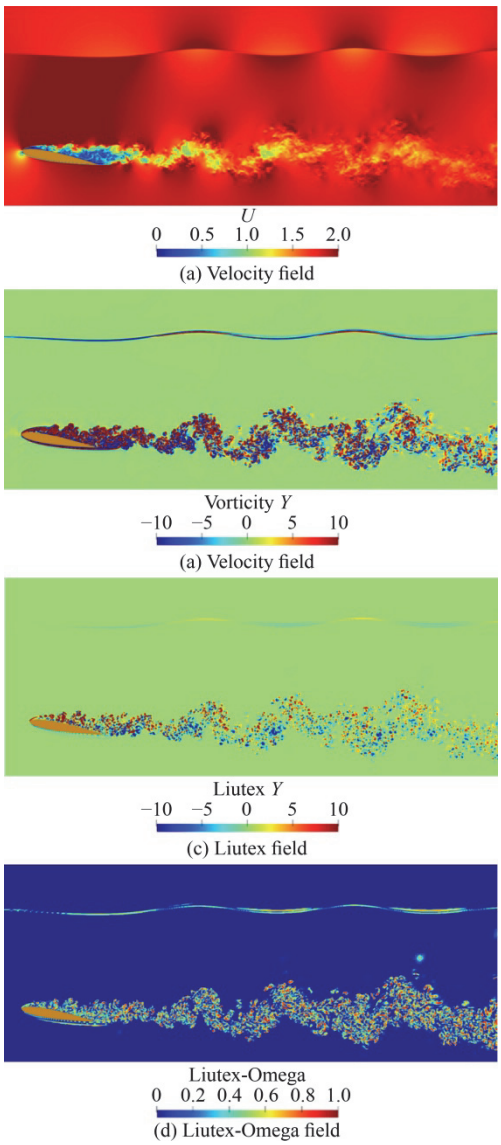

Fig. 3 Comparison of flow field in Y section

In this study, the hydrofoil's submersion depth is $h/c = 0.3,\ 1.3$, and the incoming flow velocity is 1.789 m/s, corresponding to the Reynolds number $Re = \rho Uc/\mu = 1.569\times10^{6}$ and the Froude number $F_{nc} = U/\sqrt{gc} = 0.571$. The density ratio of air to water is 1/998, and the dynamic viscosity ratio is

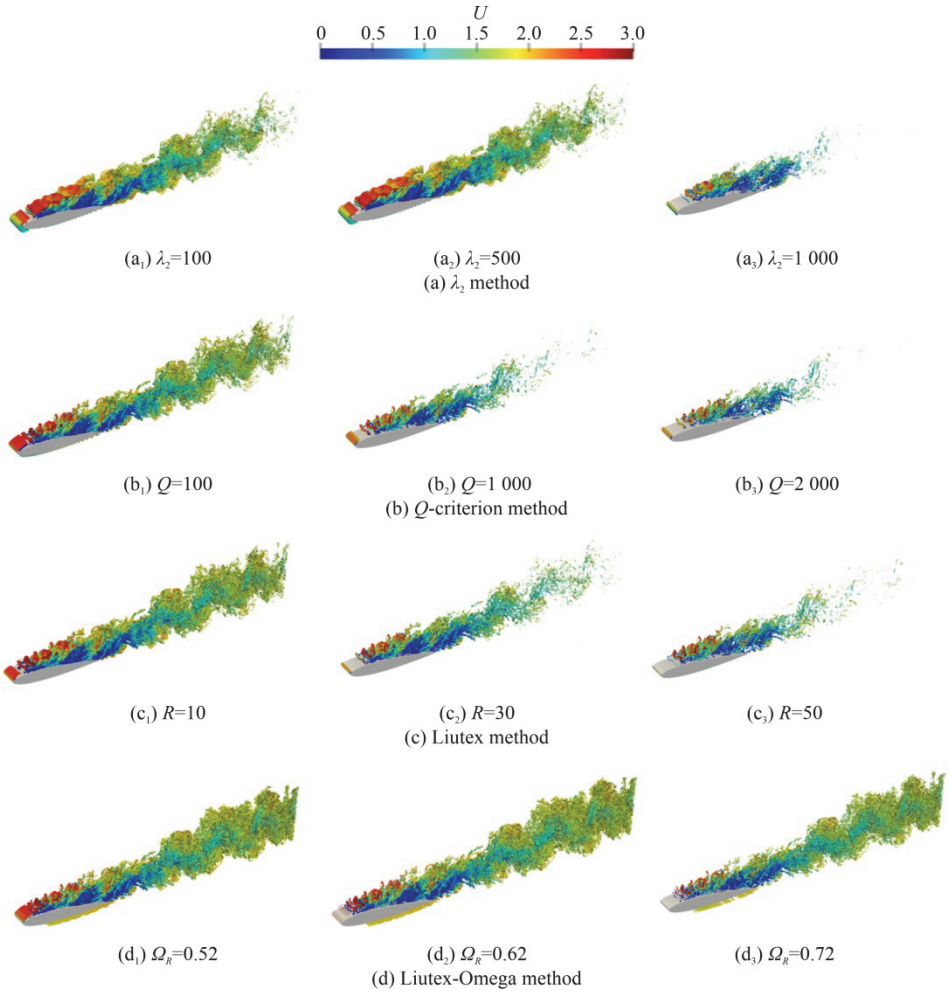

Fig. 4 Comparison of three-dimensional vortex structures identified by different methods

1.784×10^{-5} / 1.138×10^{-3}. The surface tension coefficient is 0.072 N/m, and the gravitational acceleration is $g=9.81\,\mathrm{m/s^2}$. The dimensionless time is $t^*=tU/c$, where t is the calculation time.

To capture the bubble downwash phenomenon following wave breaking, an extremely high-resolution grid is necessary. Therefore, adaptive mesh refinement technology is employed to reduce computational resource consumption. The refinement criteria include a maximum tolerance for the estimated error in the velocity field denoted as $u_{\mathrm{err}}=2\times10^{-3}$ and in the water volume fraction set as $f_{\mathrm{err}}=1\times10^{-18}$. The maximum and minimum refinement levels are 11, 6, corresponding to grid resolutions of $\Delta_{\min}=c/256$, $\Delta_{\max}=c/8$. The validation of the numerical method and more details can be found in the previous study[25]. The schematic of the mesh refinement is shown in Fig. 2. As depicted, the grid is primarily refined near the free surface, around the hydrofoil, and in the wake region, aligning with our expectations for mesh refinement.

3. Results and discussions

3.1 *Vortex comparison*

At a submersion depth of $h/c=1.3$, the hydrofoil disturbs the free surface, creating a regular wave pattern. In Fig. 3, the velocity field, vorticity field, Liutex field and Liutex-Omega field in the Y-plane are presented. From Fig. 3(a), it can be observed that due to the disturbance, the velocity in the upper region of the hydrofoil and the wake area becomes fluctuating, increasing the overall turbulence of the flow field. Figure 3(b) displays the vorticity field, revealing numerous alternating positive and negative vortex structures in the hydrofoil wake. However, compared to Figs. 3(c), 3(d), the vortex structures in the vorticity field appear quite blurred, with unclear vortex boundaries, especially around the hydrofoil. Figures 3(c), 3(d), utilizing the Liutex method and the Liutex-Omega method, effectively capture the vortex structures around the hydrofoil and in the wake region.

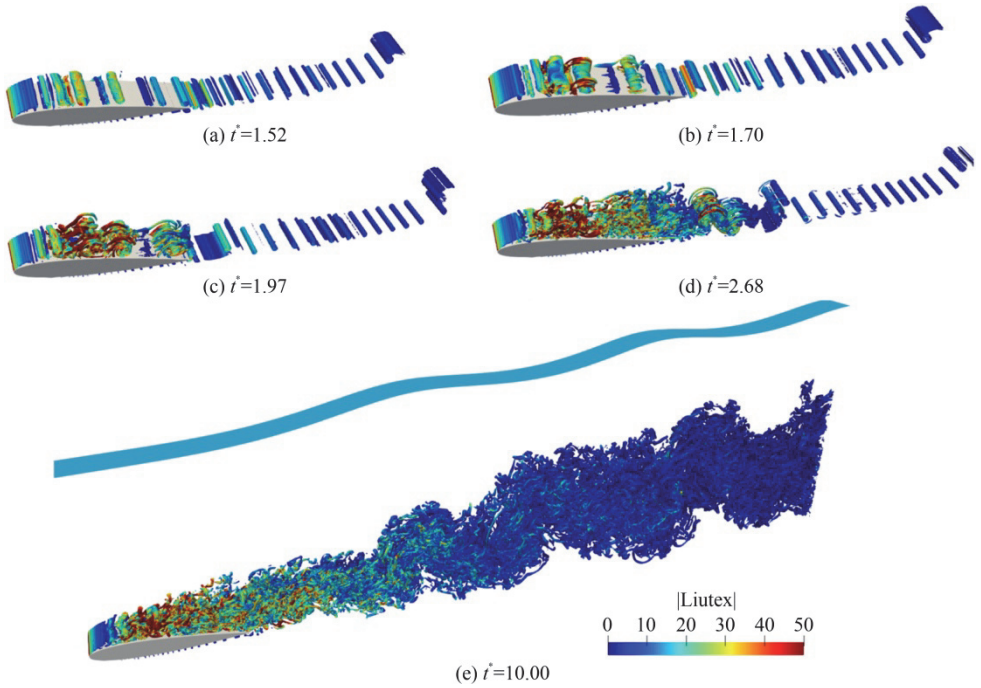

Fig. 5 Evolution of vortex structure around hydrofoil ($\Omega_R = 0.52$)

These methods provide a clearer and more defined representation of the vortex structures compared to the traditional vorticity field.

Figure 4 shows the three-dimensional vortex structures extracted using the λ_2 method, Q-criterion method, Liutex method, and Liutex-Omega method. Compared with other methods, the λ_2 method differs mainly in the upper region of the hydrofoil, where transition occurs and vortices shed. The λ_2 method forms a false vortex at the leading edge of the hydrofoil, and in the upper region, it only captures vortex tube structures, failing to identify the turbulent transition. Fig. 4(b) shows the Q-criterion method. Compared to Figs. 4(c), 4(d), the Q-criterion method has a significant threshold selection issue and cannot simultaneously display both strong and weak vortices. Overall, the Liutex method and Liutex-Omega method provide more accurate identification of vortex structures in the hydrofoil flow field. The Liutex-Omega method is particularly recommended due to its ability to solve the threshold issue[1, 20].

The evolution of vortex structures around the hydrofoil identified by the Liutex-Omega method is illustrated in Fig. 5. It can be observed that, at the submersion depth of $h/c = 1.3$, the free surface remains unbroken, and the vortex structures around the hydrofoil do not interact with the free surface. The evolution of vortex structures on the upper surface of the hydrofoil is depicted: Initial vortex tubes detach ($t^* = 1.52$), followed by the formation of vortex filaments around the tubes ($t^* = 1.70$, 1.97). These filaments expand their motion range into the hydrofoil's wake ($t^* = 2.68$), ultimately resulting in complex vortex structures downstream ($t^* = 10$). Further instantaneous vortex structures at $t^* = 10$ are presented in Fig. 6. The Liutex-Omega method effectively captures the transition process of the flow field on the upper surface of the hydrofoil, with the vector nature of Liutex allowing for the expression of the rotation axis direction of the vortex structures[26]. In the laminar region, the vortex structures attach to the leading edge of the hydrofoil in layers rotating in the same direction, subsequently forming detached two-dimensional vortex tubes. These tubes undergo gradual deformation, lifting and stretching from the leading edge, resulting in hairpin vortex structures that can induce new vortices, creating turbulent transition region. Ultimately, a fully developed turbulent region forms at the hydrofoil's trailing edge, characterized by highly complex wake vortex structures.

3.2 *Bubble dynamics*

In this part, the wave-breaking condition $h/c = 0.3$ is adopted. The volume of entrained gas over time is extracted, as shown in Fig. 7. As illustrated in Fig. 7(a), the change in entrained gas volume can be divided into three stages: The initial stage ($t^* < 4$), the rapid-developing stage ($4 \le t^* \le 8$) and the stable stage ($t^* > 8$).

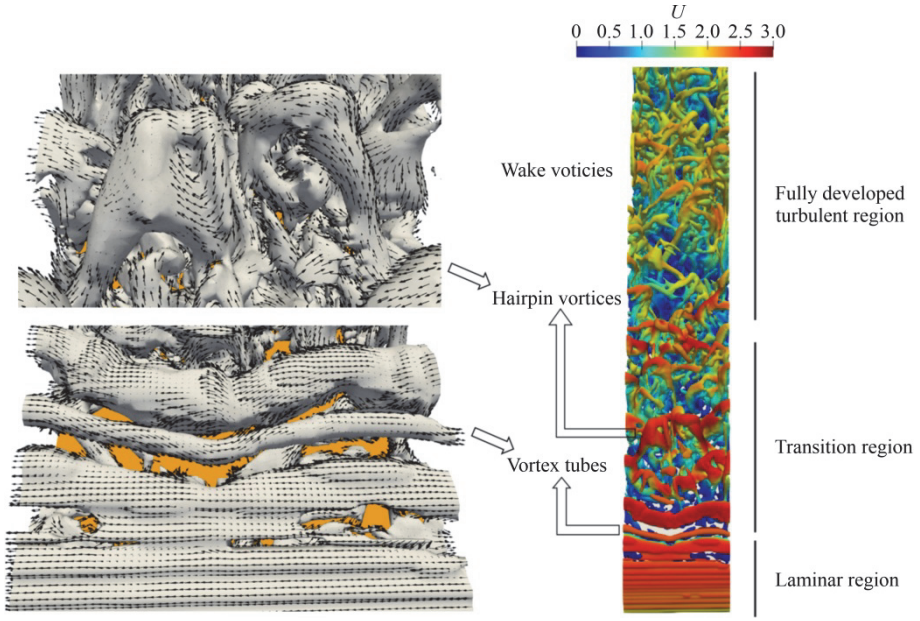

Fig. 6 Instantaneous vortex structure $t^* = 10$ $(\Omega_R = 0.52)$

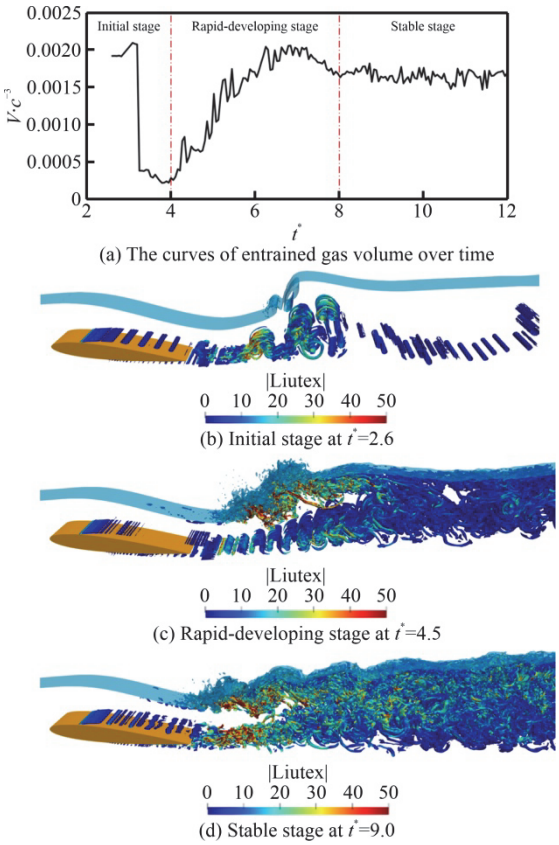

(a) The curves of entrained gas volume over time

(b) Initial stage at t^*=2.6

(c) Rapid-developing stage at t^*=4.5

(d) Stable stage at t^*=9.0

Fig. 7 Development stage of bubble entrainment $(\Omega_R = 0.52)$

In the initial stage, due to the obstruction of the hydrofoil, the wave surface continuously rises to form a leading wave. When the wave height exceeds a certain threshold, the leading wave rolls forward, entraining a large cavity. A water tongue is formed subsequently that rolls forward again, entraining a smaller cavity. As shown in Fig. 7(b), due to the upward movement of vortex structures in the hydrofoil wake, these two large cavities quickly break and escape from the free surface, causing a sudden drop in the volume of entrained gas.

In the rapid-developing stage, the upper region of the hydrofoil continuously undergoes breaking, with cavities being entrained and breaking into small bubbles, resulting in an overall increase in the total volume of entrained gas. As shown in Fig. 7(c), a large number of vortex structures form in the breaking leading wave region, and the trailing edge of the hydrofoil also forms vortices that continuously shed and mix further downstream.

In the stable stage, as depicted in Fig. 7(d), the leading wave forms a continuously breaking two-phase mixing zone, but the overall volume of entrained gas remains relatively stable. Additionally, in this stage, the vortex structures from the hydrofoil no longer exhibit distinct shedding due to the influence of free surface vortex structures. Instead, they mix with the vortices generated by wave breaking, forming a more chaotic vortex region.

Figure 8 shows the temporal variation in the total number of entrained bubbles, which also corresponds to the three stages described in Fig. 7. In the initial stage, due to the relatively mild breaking of the free surface and the larger volume of entrained bubbles, the overall number of bubbles is low. In the rapid-developing stage, the large cavities entrained in the

previous stage rapidly break up, forming a large number of small bubbles. During this stage, the intensity of free surface breaking increases continuously, leading to a rise in the total volume of entrained gas and an increase in the number of bubbles. Consequently, the number of bubbles shows a rapid upward trend in this stage. In the stable stage, the total volume of gas entrained in the flow field remains relatively stable, and the number of bubbles maintains a high value.

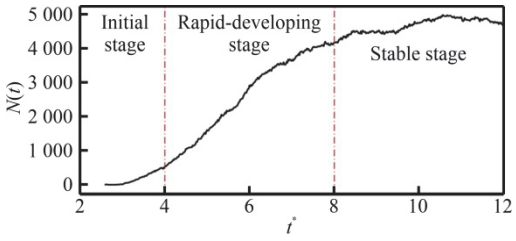

Fig. 8 The curves of bubble number over time

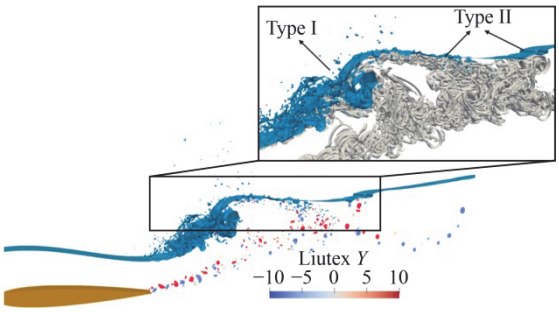

Fig. 9 The instantaneous vortex structure at $t^* = 3.76$ ($\Omega_R = 0.52$)

Regarding the mechanisms of air entrainment, two types have been observed: Types I, II. Figure 9 shows the Liutex field in the Y-plane at $t^* = 3.76$. From this figure, we can observe the upward motion of vortex pair structures generated at the trailing edge of the hydrofoil, which impacts the free surface. Type I entrainment is primarily caused by the obstruction effect of the hydrofoil and is the main source of gas entrainment in the flow field. However, by examining the vortex structures using the Liutex-Omega method, we find that this portion of entrained gas is influenced by the upward-moving vortex structures at the trailing edge of the hydrofoil, limiting its downstream movement and complicating its dynamics. Type II entrainment is mostly caused by the hydrofoil wake's vortex pair structures moving upward and reaching the free surface, which rolls and entrains gas.

The time-averaged bubble size spectrum is calculated using the following equation:

$$r_{\text{eff}} = \left(\frac{3v_b}{4\pi}\right)^{1/3} \tag{22}$$

$$\bar{N}(r_{\text{eff}}) = \frac{1}{T}\int_t^{t+T} \frac{n(r_{\text{eff}}, b)}{b}\,\mathrm{d}t \tag{23}$$

$$\bar{N}_0 = \int_0^{r_{\max}} \bar{N}(r_{\text{eff}}, b)\frac{4}{3}\pi r^3 \mathrm{d}r \tag{24}$$

where b is the total computational domain, v_b is the volume of a single bubble.

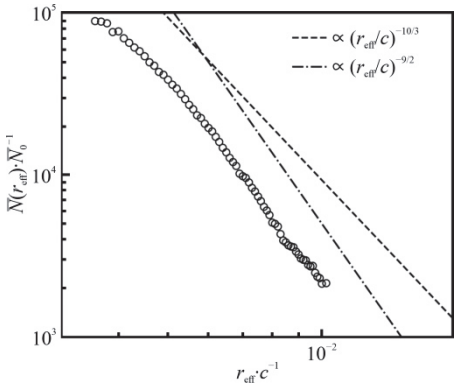

Fig. 10 Time-averaged bubble particle size spectrum

As shown in Fig. 10, we observe that the bubble size distribution follows a power-law distribution. This is due to the fact that the bubbles are produced through wave breaking, and the main motion feature of the bubble population is shear-induced breaking. Previous studies[27-28] have demonstrated that the bubble size distribution resulting from pure wave breaking follows a –10/3 power-law distribution. In this study, as the bubble volume increases, the slope of the bubble size distribution also increases. This trend is similarly observed in bubbles generated by the breaking of flow around structures penetrating the free surface[7-8, 29-30]. In our study, this phenomenon is mainly influenced by the vortex pairs in the hydrofoil wake. Figure 11 shows the vortex pair structures at $t^* = 10$. The upward motion of the hydrofoil's vortex pairs can be found clearly, which impacts the bubbles in the flow field. This effect is particularly significant for larger bubbles, causing them to quickly escape from the free surface or break up, thereby reducing their residence time in the water. At the same time, small bubbles are swept down deeper, In the size spectrum, this results in a decrease in the number of large bubbles and a shift in the bubble size distribution slope from –10/3 to –9/2.

4. Conclusions

In this study, the third-generation vortex identification method is embedded into the incompressible

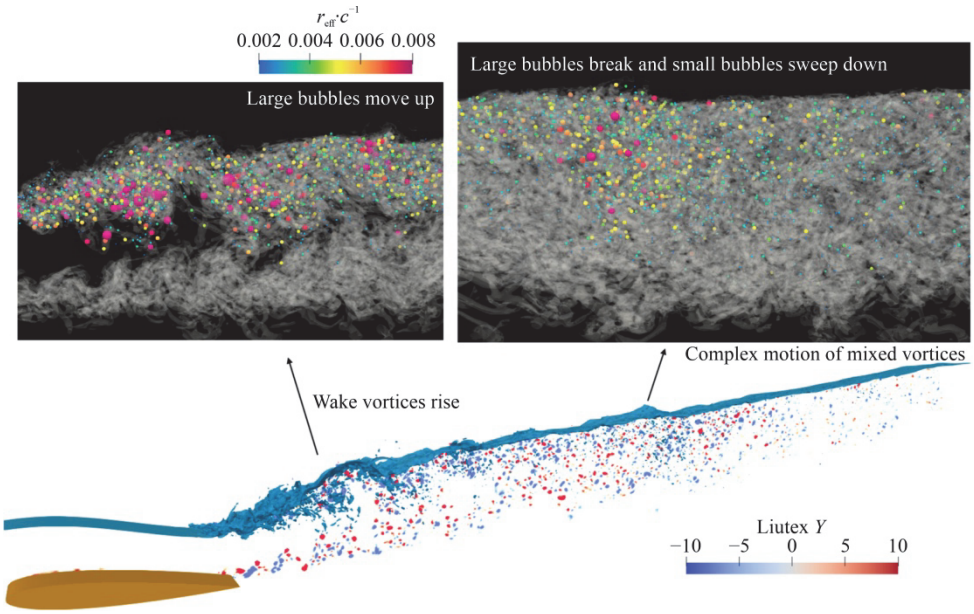

Fig. 11 The instantaneous vortex structure at $t^* = 10$ $(\Omega_R = 0.52)$

multiphase flow solver Basilisk to analyze the flow field structure and bubble entrainment phenomena around a shallowly submerged hydrofoil. Using adaptive mesh refinement technology, we simulate the flow field structures around the hydrofoil at two submersion depths, $h/c = 0.3$, $h/c = 1.3$. The third-generation vortex identification technology is employed to explain the bubble entrainment phenomena in the flow field. The main conclusions of this paper can be summarized as follows:

(1) Compared to other vortex identification methods, the third-generation vortex identification technology provides better identification results, particularly the Liutex-Omega method, which effectively addresses the threshold selection problem.

(2) Two mechanisms of air entrainment, types I, II, are observed. Using the Liutex method, it is found that the wake vortex structures in the hydrofoil directly cause type II, and they also have an impact on type I bubble entrainment motion.

(3) The upward motion of the hydrofoil wake vortex structures causes large bubbles in the flow field to quickly rise or break, reducing their residence time in the water. As bubble size increases, the slope of the bubble size spectrum shifts from –10/3 to –9/2.

Acknowledgment

This work was supported by the Research and Application Demonstration Project of Key Technologies for Safeguarding of Container Vessels in Ningbo Zhoushan Port Based on Intelligent Navigation (Grant No. ZJHG-FW-2024-27).

Conflict of interest

All authors declare that there are no other competing interests.

References

[1] Zhao W., Wang J., Wan D. Vortex identification methods in marine hydrodynamics [J]. *Journal of Hydrodynamics*, 2020, 32(2): 286-295.

[2] Dong X., Gao Y., Liu C. New normalized Rortex/vortex identification method [J]. *Physics of Fluids*, 2019, 31(1): 011701.

[3] Liu C., Ahmari H., Nottage C. et al. Liutex and third generation of vortex definition and identification (Liutex and Third Generation of Vortex Identification: Workshop from Aerospace and Aeronautics World Forum 2021) [M]. Singapore: Springer Nature, 2023, 3-23.

[4] Liu C., Gao Y., Tian S. et al. Rortex-A new vortex vector definition and vorticity tensor and vector decompositions [J]. *Physics of Fluids*, 2018, 30(3): 035103.

[5] Liu C., Gao Y., Dong X. et al. Third generation of vortex identification methods: Omega and Liutex/Rortex based systems [J]. *Journal of Hydrodynamics*, 2019, 31(2): 205-223.

[6] Di Giorgio S., Pirozzoli S., Iafrati A. On coherent vortical structures in wave breaking [J]. *Journal of Fluid Mechanics*, 2022, 947: A44.

[7] Li Z., Liu C., Wan D. et al. High-fidelity simulation of a hydraulic jump around a surface-piercing hydrofoil [J]. *Physics of Fluids*, 2021, 33(12): 123304.

[8] Hu Y., Wu J., Wan D. et al. Preliminary control of the air entrainment in bow wave based on the Liutex force method [J]. *Journal of Hydrodynamics*, 2022, 34(3): 483-490.

[9] Hu Y., Liu C., Hu C. et al. Numerical investigation of flow structure and air entrainment of breaking bow wave generated by a rectangular plate [J]. *Physics of Fluids*, 2021, 33(12): 122113.
[10] Hu Y., Liu C., Zhao M. et al. High-fidelity simulation of an aerated cavity around a surface-piercing rectangular plate [J]. *Physical Review Fluids*, 2023, 8(4): 044003.
[11] Yu H., Wang Y. Liutex-based vortex dynamics: A preliminary study [J]. *Journal of Hydrodynamics*, 2020, 32(6): 1217-1220.
[12] Wang Y., Yu H., Zhao W. et al. Liutex-based vortex control with implications for cavitation suppression [J]. *Journal of Hydrodynamics*, 2021, 33(1): 74-85.
[13] Zhao W., Wang Y., Chen S. et al. Parametric study of Liutex-based force field models [J]. *Journal of Hydrodynamics*, 2021, 33(1): 86-92.
[14] Popinet S. An accurate adaptive solver for surface-tension-driven interfacial flows [J]. *Journal of Computational Physics*, 2009, 228(16): 5838-5866.
[15] Popinet S. A quadtree-adaptive multigrid solver for the Serre–Green–Naghdi equations [J]. *Journal of Computational Physics*, 2015, 302: 336-358.
[16] Liu S., Wang H., Bayeul-Lainé A. C. et al. Wave statistics and energy dissipation of shallow-water breaking waves in a tank with a level bottom [J]. *Journal of Fluid Mechanics*, 2023, 975: A25.
[17] Hashemi M., Shalbaf S., Jadidi M. et al. Effects of gas viscosity and liquid-to-gas density ratio on liquid jet atomization in crossflow [J]. *AIP Advances*, 2023, 13(3): 035105.
[18] Sykes T. C., Cimpeanu R., Fudge B. D. et al. Droplet impact dynamics on shallow pools [J]. *Journal of Fluid Mechanics*, 2023, 970: A34.
[19] Liu J., Gao Y., Liu C. An objective version of the Rortex vector for vortex identification [J]. *Physics of Fluids*, 2019, 31(6): 065112.
[20] Xu W., Gao Y., Deng Y. et al. An explicit expression for the calculation of the Rortex vector [J]. *Physics of Fluids*, 2019, 31(9): 095102.
[21] Liu C., Gao Y., Dong X. et al. Third generation of vortex identification methods: Omega and Liutex/Rortex based systems [J]. *Journal of Hydrodynamics*, 2019, 31(2): 205-223.
[22] Duncan J. H. The breaking and non-breaking wave resistance of a two-dimensional hydrofoil [J]. *Journal of Fluid Mechanics*, 1983, 126: 507-520.
[23] Pernod L., Sacher M., Wackers J. et al. Free-surface effects on two-dimensional hydrofoils by RANS-VOF simulations [J]. *Journal of Sailing Technology*, 2023, 8(1): 24-38.
[24] Jin Q., Hudson D., Temarel P. et al. Turbulence and energy dissipation mechanisms in steady spilling breaking waves induced by a shallowly submerged hydrofoil [J]. *Ocean Engineering*, 2021, 229: 108976.
[25] Shao Y., Wang W., Wan D. et al. Numerical investigations of breaking waves and air entrainment induced by a shallowly submerged hydrofoil [J]. *Ocean Engineering*, 2024, 312: 119026.
[26] Gao Y., Liu J., Yu Y. et al. A Liutex based definition of vortex rotation axis line [J]. *Journal of Hydrodynamics*, 2019, 31(3): 445-454.
[27] Deane G. B., Stokes M. D. Scale dependence of bubble creation mechanisms in breaking waves [J]. *Nature*, 2002, 418(6900): 839-844.
[28] Deike L. Mass transfer at the ocean–atmosphere interface: The role of wave breaking, droplets, and bubbles [J]. *Annual Review of Fluid Mechanics*, 2022, 54(1): 191-224.
[29] Zhang X., He K., Wan D. Research progress on mechanism and numerical simulation methods of water-air-bubble mixed flow around marine structure [J]. *Chinese Journal of Ship Research*, 2022, 17(3): 1-28.
[30] Li Z., Zhang X., Wan D. Research progress on the hydrodynamic performance of water-air-bubble mixed flows around a ship [J]. *Journal of Hydrodynamics*, 2022, 34(2): 171-188.